Supplementary materials for Facies vectors: Disentangling environmental variability, diagenesis, and secular change in carbonate stratigraphies

---

Lateral variability and section correlations

A common approach to potentially circumvent the contribution of subenvironments is to measure parallel sections across a fossil platform to give evidence that a signal stems from a broader trend. However, with migrating lateral variability as a major source of stratigraphic excursions—manifest in fossil assemblages, chemostratigraphic peaks and nadirs, or lithostratigraphic observations—the data upon which correlations rely likely are diachronous (Supplementary Figure 1). For instance, subaerial exposure markers (Hillgaertner, 1998), flooding surfaces (Goldhammer et al., 1991), and distinctive stromatolite occurrences (Hofmann, 1977) are common markers for correlating sections. However, assuming that the entire platform was synchronously exposed or covered by a uniform layer of stromatolites is, in itself, an interpretation of large-scale secular change. A more neutral starting point based upon current knowledge of modern platforms would be to say that prograding, exposed islands, and the unique conditions for distinctive stromatolites existed on some portion of the platform throughout some of its history. As part of the platform's environmental mosaic, these conditions can to be sampled by separate sections, but their occurrences most likely track migration.

This concept of surface diachroneity is not new, as this limitation often is acknowledged in sequence stratigraphic frameworks of fluvial-deltaic environments (Wagoner et al., 1988) or depositional models for long-term cycles on carbonate platforms driven by eustatic sea-level change Sarg (1988). Studies of modern environments, however, now indicate that the assumption of diachroneity should apply even to chemical excursions (Geyman and Maloof, 2021) and short-term environmental transitions (Dyer et al., 2018, Geyman et al., 2021)

These complications for correlation exist regardless of the relative distance separating sections. When parallel columns are nearby, separated by less than the lengthscale of variability and track similar facies bodies (possibly the migration of the same stromatolite belt), their signals will have high correspondence, but be offset in time (Figure 1A–C). Therefore, even if a geologist can trace a bed over continuous outcrop for tens of kilometers, correlations have a temporal precision limited by rates of facies migration or platform subsidence (Drummond and Wilkinson, 1993, Burgess, 2001, Geyman et al., 2021). When sections are separated by more than the lengthscale of variability, alignment no longer stems from the passing of the same depositional bodies and relies upon similar sequences of excursions (Figure 1D). On carbonate platforms, similar cycles of depositional facies are expected to be pervasive, as shallowing-up parasequences can result from autogenic processes (Geyman et al., 2021, Burgess, 2001), which gives a mechanism by which even distant stratigraphies can be correlated through signals that neither are linked in cause, nor time. In either case of section alignment, sub-environmental variability remains as the likely origin of the signal, and so we still must answer a key question: What is the contribution of the local sub-environment that deposited each bed to the overall trend we see in the stratigraphy?

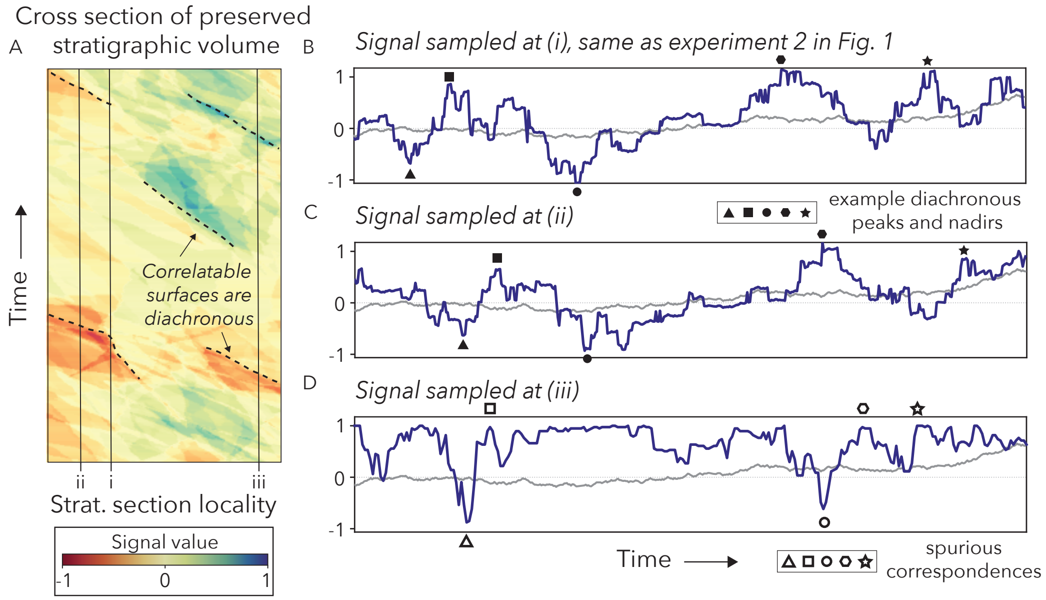

Supplementary Figure 1: Experiments from Figure 1 (main text) also illustrate how attempting to correlate parallel sections does not relieve ambiguity in assessing secular trends. (A) In a cross section of the preserved stratigraphic volume from experiment 2 in Figure 1 (main text), we see that surfaces representing extreme peaks and nadirs (and therefore the most recognizable for correlation) stem from lateral variability and are diachronous. (B,C) When we plot the signals from two parallel sections that are separated by less than the spatial lengthscale of variability, the most extreme peaks and nadirs that would be used for correlation are not part of the original signal and are offset in time. For this system, correlating parallel sections would not help disentangle local and secular changes, and would simply identify the migration of internal variabilities. (D) A signal that is separated from *i* and *ii* by more than the lengthscale of variability does not sample the same facies migrations. One could apply a null hypothesis that signals should correlate and assume differential accumulation rates that would dilate and contract this record to spuriously align sections, but correspondence would only relate to the passing of similar depositional conditions in a comparable sequence.

Diagenesis

Dissimilar to weather and climate data, carbonate stratigraphies also are subject to diagenesis, which occurs after the depositional recording of signals. Once a rock starts to form from sediments, it will be exposed to varying degrees of alteration from factors like early stage fluid flow (Higgins et al., 2018, Ahm et al., 2018) or the influence of basinal fluids at great depths (Swart, 2015, Derry, 2010). Similar to depositional facies, variable exposure of rocks to these alteration factors also can create signals of relatively high magnitude compared to any expected secular change. Even just early stage flow of meteoric waters through Bahamian carbonates drives an additional ∼5‰ variability such that just the last 20 thousand years of stratigraphy on the GBB can replicate the scale of change seen in δ^{13}C values over the last two billion years (Geyman and Maloof, 2021).

Although recent attention mostly has been given to the impacts of post-burial diagenesis on chemical measurements in carbonates, these processes also are well known to alter fossil occurrences and physical sedimentological data. For an organism's remains to survive burial and exhumation and eventually be tabulated by a paleontologist, its taphonomic window must align with the diagenetic forces at play to leave a recognizable portion preserved in a way that can be identified (Behrensmeyer et al., 2000, Kidwell et al., 2005). For example, trilobite species counts are impacted both by needing to be buried in an environment that does not dissolve or crush calcitic exoskeletons, and within a facies that can be split open to view enough diagnostic features for identification (Hughes, 1995). By the same token, the carbonate grains that are observed by a geologist to estimate size distribution or phase modalities can be altered by burial processes that may preferentially destroy or distort certain grain sizes, porosities, and/or mineralogies (Coogan and Manus, 1975).

Correlations between qualitative lithofacies and δ^{13}C values in an extended lower Cambrian record

Even with shortcomings, qualitative lithologies motivate deeper investigation of the influence of depositional environments on carbonate signals. As an example, we perform an exercise on the Moroccan Sidi Msal section and its record of δ^{13}C values from Maloof et al. (2010b, Supplementary Figure 2), which often are used as a backbone to correlate global early Cambrian timescales and interpret broader changes in the carbon cycle and ocean oxygenation state (Dahl et al., 2019, Maloof et al., 2010a, Betts et al., 2018, Hay et al., 2019, Smith et al., 2016). Given the relative proportions of categorical facies in the Moroccan sections (Maloof et al., 2010b,a, 2006), we can picture this ancient platform with migrating facies bodies as potential sources of sub-environmental variability (Supplementary Figure 2A). As a first pass in understanding the influence of depositional conditions without *a priori* knowledge of δ^{13}C distributions on the fossil platform, we look at the relative proportions of qualitative facies categories throughout the section, compared to the isotope curve. We find that the majority of noted peaks and nadirs in the record of δ^{13}C values are matched by a peak in prevalence of at least one lithology (Supplementary Figure 2C). The high degree of correlation between local facies descriptions and δ^{13}C values (Supplementary Figure 2D) in a central outcrop for interpreting Cambrian global change, points to the need to develop fine-scale quantitative lithofacies methods to help dis-

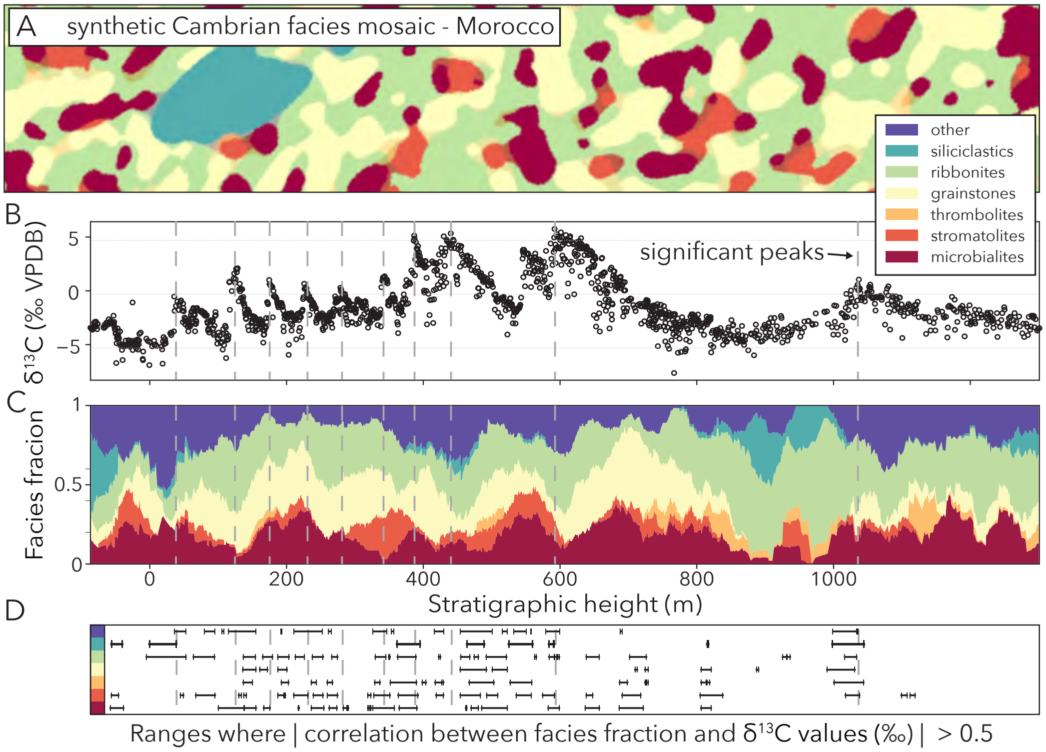

Supplementary Figure 2: An exercise investigating the relationship between lithology and δ^{13}C values in the Moroccan Sidi Msal section from Maloof et al. (2010b). (A) The proportion of qualitative facies groups reported in these sections (Maloof et al., 2006, 2010b), create a schematic of what the facies mosaic and sources of spatial variability may have looked like on the ancient platform. (B) The Sidi Msal record of δ^{13}C values from Maloof et al. (2010b) provides and expanded record of δ^{13}C that covers much of the lower Cambrian. (C) After compiling proportions of the major categorical lithologies in a moving 50 meter window, we find that key features of the record of δ^{13}C values are reflected in peaks or nadirs of one or more facies groups. For instance, six of the ten major peaks in δ^{13}C values are matched with local maxima in the occurrences of microbialites. (D) This visual correspondence also is reflected in statistical correlations between the facies proportions and δ^{13}C values in 50 meter moving windows, where ten of eleven peaks occur during intervals with high Pearson coefficients for at least two facies groups.

entangle these relationships. We need to be able to approach questions like: What proportion of peaks and nadirs in the record of δ^{13}C values are fully explained by the migration of variable facies and are thus diachronous locally, and not related globally? Of the early Cambrian excursions in δ^{13}C values that remain as global and synchronous, are any caused by broad, coordinated shifts in facies that could be expected by an event like sea level rise and are not related to carbon cycling? The remainder of this study aims to introduce means by which we may start to answer such questions.

Stewart's Mill geochronology

Based upon trilobite biostratigraphy, the Stewart's Mill locality falls within the Montezuman Stage of the Waucoban Series (Laurentian equivalent of the global Series 2; Hollingsworth, 2011). The Montezuman stage has no absolute radiometric age constraints , but current estimates from detrital zircon studies, sedimentation rate modeling, and species duration estimates give a maximum span of 5 million years from approximately 519 to 514 million years ago (Peng et al., 2020, Karlstrom et al., 2018, Sundberg et al., 2020). The lower member of the Poleta Fm is stratigraphically thin compared to the siliciclastic Campito Fm (also within the Montezuman; Hollingsworth, 2011), and so the carbonates at Stewart's Mill likely only represent a small portion of the possible 5 million year duration. Estimates of time scale for accumulation of the stratigraphy we study at Stewart's Mill are highly uncertain, but these strata may represent 1 million years or less.

Polished slab preparation and imaging

Sample preparation

In preparing polished slabs for imaging, we track cut face orientation in reference to faces marked in the field such that relative orientation of each image, with respect to stratigraphic up and local bedding planes, can be accounted for when assigning metrics. We start by cutting a billet that is large enough to fill the entire ∼4.4 × 5.5 cm camera field of view (FOV), or as large as possible given the sample size. Following cutting the billet, we loosely place all cut pieces back together and put the entire sample in a sand box to orient it back to field position as indicated by the strike-dip mark and measurement made in the field. Keeping the billet in this position, we then expose the cut face to measure and mark its strike and dip (Supplementary Figure 3A).

This cut face of the billet with known orientation will be affixed face-down for grinding, and so the line of strike will not be visible. To track this line, we make a saw mark along the edge of the billet at the front and back of the strike arrow and paint in these saw marks with red to mark the front and white to mark the back (Supplementary Figure 3B). With orientation adequately marked, we affix each billet to a steel plate with 2 ton epoxy and allow 48 hours or longer to cure. The steel plate both acts to increase the robustness of final polished slabs as an archive and allows us to secure slabs to a magnetic chuck for surface grinding.

We grind the affixed billets with a Mitsui MSF-818PC-NC CNC surface grinder equipped with a 320 grit diamond wheel, which is the same grinding setup used for 3D modeling with the Grinding Imaging, and Reconstruction

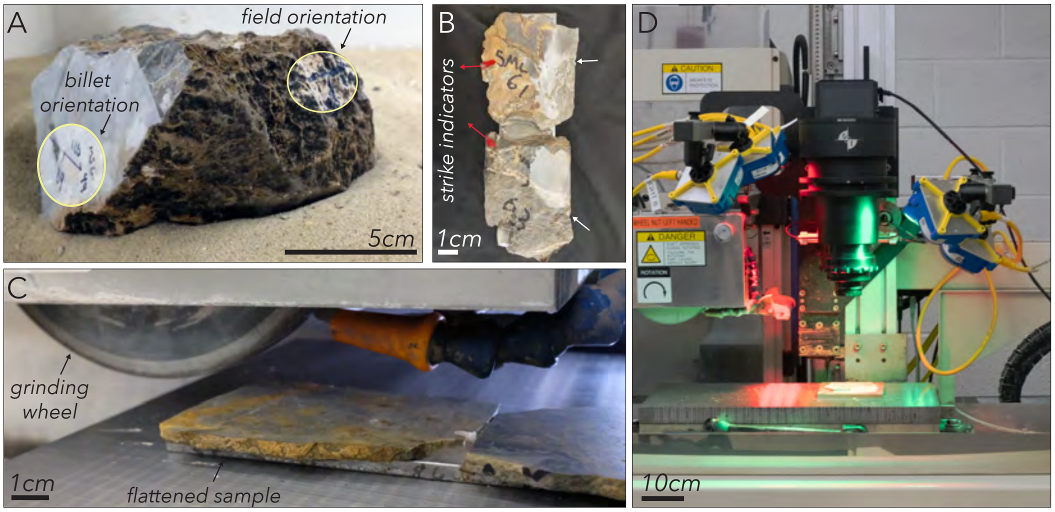

Supplementary Figure 3: Grinding and imaging methods. (A) We place cut billets in a sandbox, rotate into their outcrop orientation based upon strike-dip marked in the field, and mark the orientation of the billet's cut face. (B) Prior to grinding, we mark the ends of the strike-dip arrow on the cut face with paint so the orientation will be constrained even after the cut face is affixed to a steel bar with epoxy. (C) We use a CNC surface grinder to grind all samples flat and parallel. (D). Once samples are polished by hand, we image each rock with a 150 MP achromatic sensor under eight separate narrow-band LEDs to create a multi-spectral image.

Instrument (GIRI; Mehra et al., 2022). We grind each sample until enough parallel, flat area is exposed to fill the camera FOV, aiming to keep a uniform thickness across the entire sample set (Supplementary Figure 3C). Following grinding, the samples show some scratch marks from the diamond grit, and so we polish each slab by hand on a bench top for approximately one minute each with 600 and 800 grit sandpaper. Although hand polishing greatly improves the finish on each slab, we prepare each sample for imaging by applying a thin coat of mineral oil with a foam brush to reduce the specular appearance of any remaining scratches.

Sample imaging

We image samples with the GIRI camera and reflected light setup described in Manzuk et al. (2022), equipped with eight narrowband LEDs of the following wavelengths (Supplementary Figure 3D); 365 nm (UV fluorescence), 470 nm (blue), 505 nm (cyan), 530 nm (green), 590 nm (yellow), 625 nm (red), 760 nm (red edge), 940 nm (NIR). Our goal when imaging is to achieve well-exposed images across all samples and wavelengths without having to vary shutter speeds between samples. We keep exposure time constant such that we can directly compare pixel intensities from each wavelength between samples as a faithful measure of sample spectral characteristics without having to correct for relative exposure time. To achieve this goal while capturing quality images, we select a subset of six samples that generally span the qualitative lithologic variability in the set to test exposure times. We image each of the test samples with each wavelength at a range of exposure times. For each wavelength, we select the exposure time that gives the largest average spread of pixel values over the test set without any sample images appearing over or under exposed.

When imaging the full sample set, we use an ISO of 400 and an f-stop of 8. Our optimized shutter speeds for this sample set are; 365 nm - 8s, 470 nm - 0.6s, 505 nm - 0.5s, 530 nm - 0.5s, 590 nm - 0.8s, 625 nm $\frac{1}{3}$s, 760 nm - 0.5s, 940 nm - 0.6s. The room is kept completely dark throughout imaging such that the only light in photographs comes from the reflection of the narrowband LEDs. The camera is attached directly to the surface grinder, and so we place samples on the magnetic chuck for imaging and use the grinder controls to move samples into the FOV. Because we know all samples are ground parallel with respect to the chuck with constant thickness, we ensure that all images are well focused, even with the narrow depth of field for the camera. An automated program written in Matlab interfaces with the camera and lights to take all images automatically in sequence.

We image all samples with a Phase One IQ4 150-megapixel digital back with sensor dimensions of 4.04 × 5.37 cm. We use a 120 mm Schneider Kreuznach apochromatic macro lens, which gives a field of view and pixel resolution equal to the dimensions of the digital back. The final spatial resolution in these images is 3.76 μm per pixel.

As mentioned in Manzuk et al. (2022), these sample images suffer from some chromatic aberration, whereby each wavelength achieves maximal sharpness at a different focal depth due to the wavelength dependence of light refraction. In our imaging protocol, we keep 530 nm (green) as the maximally sharp wavelength, and model the blur in all subsequent wavelengths using the protocols of Manzuk et al. (2022). Deconvolving to resharpen images is computationally expensive, and so we only apply this operation when sharpness in a separate wavelength is expressly necessary.

Sample spectral signature

The first basic property of a rock sample that is useful for distinction and categorization is color—both what we can see with our eyes, as well as additional spectral characteristics of minerals that are invisible to humans. For example, in our samples the amount of microbialite is indicated by dark blue hues, and overall UV fluorescence tracks the degree of recrystallization. Our standardized imaging protocols across all samples already assure we

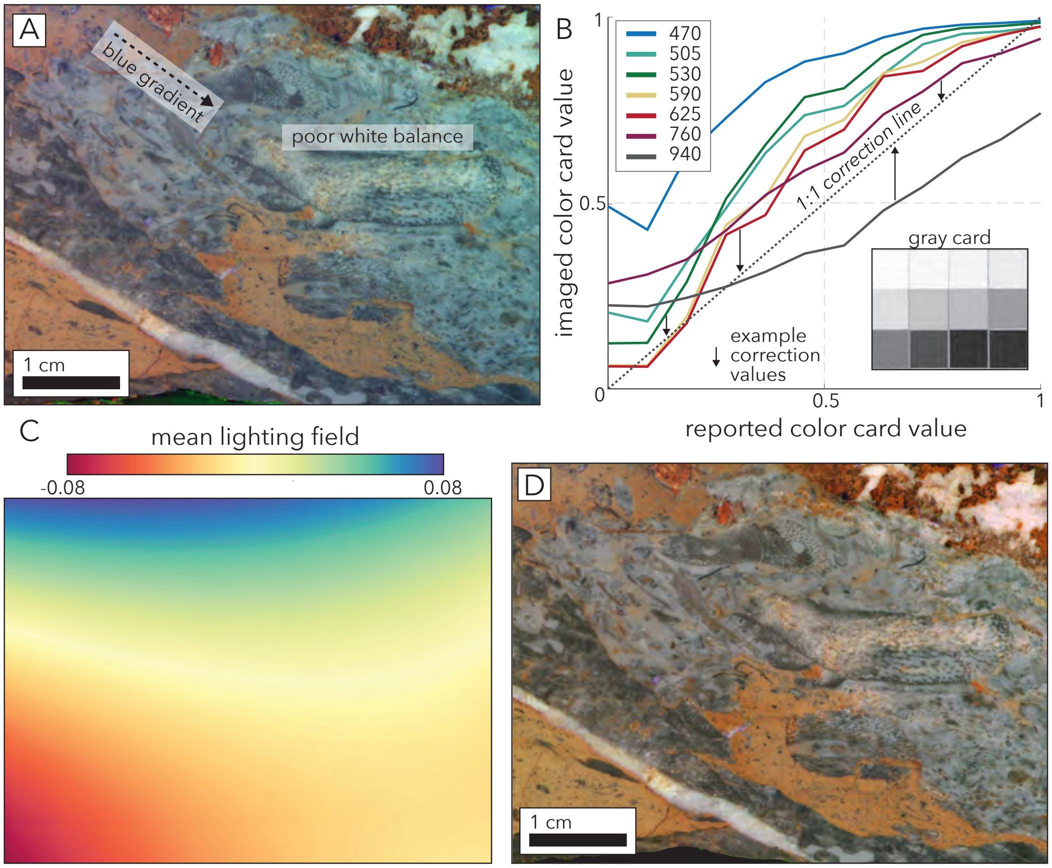

Supplementary Figure 4: Protocols for white balance and correcting lighting unevenness to assure accurate assessment of relative color over samples. (A) An example red-green-blue composite assembled from the raw images shows both the poor white balance and color gradients that result from imaging conditions. (B) The difference between the reported value for each gray level, and the actual value recorded by the camera sensor serves as a correction factor tailored across all wavelengths. (C) An example surface fit to the mean lighting field for 470 nm (blue) shows the unevenness in intensity with a general gradient that runs away from the light source, which was situated to the upper left of all samples. This surface serves as a pixel-wise correction factor with which we subtract to correct for the exact nature of lighting unevenness for each wavelength. (D) After white balancing and correcting for lighting unevenness, we achieve realistic composite images that are ready for color comparison and other quantitative analyses.

have comparable color signals, but we perform some corrections to make our images a petrographic record that is faithful to the geologist's eye and removes some imperfections.

Because our imaging protocols do not keep exposure times constant across all wavelengths, and the intensity of light from each LED that reaches the sample may vary, the colors in our raw images are not balanced. So, a gray patch of a sample, which should have an even reading for each wavelength, instead appears as whichever color has the highest combination of light intensity and exposure time (often blue in our images; Supplementary Figure 4A). To achieve white/gray balanced images, we image a matte ColorGauge Micro target under the same lighting and exposure settings used for samples, specifically looking at the twelve squares that show black, various grays, and white. We get the mean color values for each square, over each wavelength, and interpolate to get a curve through these gray levels (Supplementary Figure 4B). The difference between our experimental curves, and interpolated reported gray values from the target, serve as correction factors that redistribute pixel values to be balanced across wavelengths and produce more realistic composite images (Supplementary Figure 4D). We keep these corrections constant across samples to maintain color as a meaningful metric for comparing lithofacies.

This sample set was imaged with only a single LED for each wavelength and so the raking light is of slightly uneven intensity across the camera FOV (the narrowband light source for the imaging setup has since been changed to a ring light to improve evenness and reduce specularity). To correct this pattern and assure that all parts of the sample image have equal expression of relative brightness, we assess the mean lighting field for all wavelengths to be the mean of all sample images (Supplementary Figure 4C). Because some samples do not fit the full field of view, the edges of the mean image are less reliable, so we fit a surface to the center of the mean image to extrapolate to the edges. This surface then gives a correction value to add or subtract to each pixel based upon its location in the image. Once corrected, we successfully remove any color gradients on samples that result from uneven lighting (Supplementary Figure 4D).

Following our imaging protocols and color corrections, we have multispectral images that are a faithful record of sample color to be input to quantitative lithofacies comparison.

Geochemical measurements

Measurement of $\delta^{13}C$ and $\delta^{18}O$ values

We place approximately 0.25 mg (measured volumetrically via a laboratory standard) of sample powders in individual borosilicate reaction vessels, heat to 110 °C to remove volatiles, and cap the vessels. We then flush the vials with He to remove atmospheric gas and react the powders with five drops of H_3PO_4. We measure the CO_2 analyte with a Sercon IRMS coupled with a GasBench II sampling device. To monitor precision and accuracy of our measurements of δ^{13}C and δ^{18}O values, we analyze 15 standards (IAEA-603, $n = 4$, as well as two laboratory standards, $n = 2$ and 9 respectively, with known δ^{13}C and δ^{18}O values) for every 57 samples.

To reduce data and report final δ^{13}C and δ^{18}O values with uncertainties, we regress the δ value versus area for seven peaks per sample and standard. This regression, sometimes referred to as a linearity or peak size correction, corrects for differences in sampling peak intensity arising from volumetric measurement or mineralogical differences between analytes (Dunn and Carter, 2018). We report δ^{13}C and δ^{18}O values in standard delta notation relative to the Vienna Pee Dee Belemnite (V-PDB). To convert to V-PDB values, we use the average conversion given by IAEA-603 (δ^{13}C = 2.46‰ ± 0.01, δ^{18}O = -2.37‰ ± 0.25) and our internal VTS standard (δ^{13}C = -1.48‰ ± 0.07, δ^{18}O = -8.54‰ ± 0.14). The values we report for mean value and precision of the VTS standard come from internal long-term laboratory averages and standard deviations (n = 2,550). Our laboratory reproduces the reported values for IAEA-603 on the long term long-term with a precision of <0.09 for δ^{13}C and <0.16 for δ^{18}O(1σ, n= 145).

Our laboratory tolerances in terms of standard deviation of δ value over a single run in order to use a standard for conversion are ± 0.1‰ for δ^{13}C values and ± 0.25‰ for δ^{18}O values. In 3/19 machine runs, the IAEA standard was found to give values outside of laboratory tolerances. In such cases, we use a single point correction with VTS as the more reproducible standard for that run. We measure single replicates for each sample. In cases where the standard deviation for a sample's seven peak measurements (following correction for peak area via regression) exceeds our laboratory tolerances, we measure a duplicate and only report values for samples that achieve our precision tolerances.

Minor and trace element measurements

These measurements are made on the same sampled powders as the measurements of stable isotope ratios. For each sample, we react 1–5 mg of carbonate powder with a 0.25M buffered acetic acid solution (pH ∼ 5; Reagents are TraceMetal Grade Ammonium Hydroxide, and TraceMetal Grade Acetic Acid, Glacial from Fisher Chemical - Fisher Scientific Company, LLC.) in a 15 mL Falcon tube, using approximately 1 mL of solution per 1 mg of powder. Prior to use, we acid wash the Falcon tubes in 2% HNO_3, rinse thoroughly with 18.2 $M\Omega\cdot$ cm Milli-Q water, and allow to dry. We leave the sample-acid mixtures to digest for four hours in a sonicator, and then centrifuge the tubes for 30 minutes at 2500 rpm. We then transfer the supernatant liquid to a second acid-washed Falcon tube for analysis. This digestion method readily dissolves carbonates but leaves insoluble material, like clays and metal oxides, thereby minimizing ion extraction from co-occurring silicate minerals (Tessier et al., 1979).

We measure minor and trace element concentrations with Thermo Fisher I-Cap Q inductively coupled plasma mass spectrometer (ICP-MS). To quantify elements spanning a wide range of concentrations, we analyze each sample at two dilution levels prepared in 2% ultra-trace HNO_3. We prepare a low-concentraton aliquot at 50-fold dilution and a higher-concentration aliquot at 17-fold dilution. The less-dilute (17-fold) solutions yielded reproducible measurements for Mg, Ca, Mn, and Fe, whereas Sr concentrations in some samples exceeded the calibration range at this dilution level. The higher diultion (50-fold) solutions consistently yielded reproducible quantifications of Mg, Ca, and Sr. We report all elemental concentrations as molar ratios normalized to Ca. For each reported elemental ratio, values reflect the mean of two replicate measurements (n=2) when both dilution levels yielded results within the calibration range.

We base quantifications on four multi-element carbonate matrix-matched calibration standards. We prepare additional dilutions of these standards to produce a 10-point calibration curve spanning the concentration rage of the analyzed samples. We run all 10 calibration standards at the beginning and end of each analytical sequence, with approximately 70 unknown samples analyzed per run. We only retain samples with signal intensities within the calibration range. For a run, we require calibration curves to have an R^2 value > 0.99 for the reported analyte. We rerun samples and standards when this criterion is not met.

We internally spike all samples, standards, and blanks with ~500 ppb ^{115}In to monitor and correct for short-term instrumental drift during analysis. Each analytical run also includes four procedural blank solutions consisting of the same 2% ultra-trace HNO_3 used for sample dilution. We use these blanks for blank subtraction during data reduction.

We monitor analytical reproducibility and accuracy by repeated analysis of the NIST SRM 88b standard, included 2-4 times during each analytical run. Long-term measurements of the standard have a precision better than ±5% (1σ, n=120) for all reported elemental ratios. Our laboratory value for NIST SRM 88b is within uncertainty of accepted ratio values.

References

Ahm, A.S.C., Bjerrum, C.J., Blättler, C.L., Swart, P.K., Higgins, J.A., 2018. Quantifying early marine diagenesis in shallow-water carbonate sediments. Geochimica et Cosmochimica Acta 236, 140–159.

Behrensmeyer, A.K., Kidwell, S.M., Gastaldo, R.A., 2000. Taphonomy and paleobiology. Paleobiology 26, 103–147.

Betts, M.J., Paterson, J.R., Jacquet, S.M., Andrew, A.S., Hall, P.A., Jago, J.B., Jagodzinski, E.A., Preiss, W.V., Crowley, J.L., Birch, S.A., Mathewson, C.P., García-Bellido, D.C., Topper, T.P., Skovsted, C.B., Brock, G.A., 2018. Early Cambrian chronostratigraphy and geochronology of South Australia. Earth-Science Reviews 185, 498–543.

Burgess, P.M., 2001. Modeling carbonate sequence development without relative sea-level oscillations. Geology 29, 1127–1130.

Coogan, A., Manus, R., 1975. Chapter 3 compaction and diagenesis of carbonate sands, in: Compaction of Coarse-Grained Sediments. Elsevier. volume 18 of *Developments in Sedimentology*, pp. 79–166.

Dahl, T.W., Connelly, J.N., Li, D., Kouchinsky, A., Gill, B.C., Porter, S., Maloof, A.C., Bizzarro, M., 2019. Atmosphere–ocean oxygen and productivity dynamics during early animal radiations. Proceedings of the National Academy of Sciences 116, 19352–19361.

Derry, L.A., 2010. A burial diagenesis origin for the Ediacaran Shuram–Wonoka carbon isotope anomaly. Earth and Planetary Science Letters 294, 152–162.

Drummond, C.N., Wilkinson, B.H., 1993. Carbonate cycle stacking patterns and hierarchies of orbitally forced eustatic sealevel change. Journal of Sedimentary Research 63, 369–377.

Dunn, P.J.H., Carter, J.F., 2018. Good Practice Guide for Isotope Ratio Mass Spectrometry. 2nd ed.. FIRMS. chapter 6.4.3. p. 48. Section 6.4.3: Linearity (peak size) correction.

Dyer, B., Maloof, A.C., Purkis, S.J., Harris, P.M.M., 2018. Quantifying the relationship between water depth and carbonate facies. Sedimentary Geology 373, 1–10.

Geyman, E.C., Maloof, A.C., 2021. Facies control on carbonate δ13C on the Great Bahama Bank. Geology 49, 1049–1054.

Geyman, E.C., Maloof, A.C., Dyer, B., 2021. How is sea level change encoded in carbonate stratigraphy? Earth and Planetary Science Letters 560, 116790.

Goldhammer, R., Oswald, E., Dunn, P., Franseen, E., Watney, W., 1991. Hierarchy of stratigraphic forcing: Example from Middle Pennsylvanian shelf carbonates of the Paradox Basin. Kansas Geological Survey Bulletin 233, 361–413.

Hay, C.C., Creveling, J.R., Hagen, C.J., Maloof, A.C., Huybers, P., 2019. A library of early Cambrian chemostratigraphic correlations from a reproducible algorithm. Geology 47, 457–460.

Higgins, J.A., Blättler, C.L., Lundstrom, E.A., Santiago-Ramos, D.P., Akhtar, A.A., Ahm, A.C., Bialik, O., Holmden, C., Bradbury, H., Murray, S.T., et al., 2018. Mineralogy, early marine diagenesis, and the chemistry of shallow-water carbonate sediments. Geochimica et Cosmochimica Acta 220, 512–534.

Hillgaertner, H., 1998. Discontinuity surfaces on a shallow-marine carbonate platform (Berriasian, Valanginian, France and Switzerland). Journal of Sedimentary Research 68, 1093–1108.

Hofmann, H., 1977. On Aphebian stromatolites and Riphean stromatolite stratigraphy. Precambrian Research 5, 175–205.

Hollingsworth, J.S., 2011. Lithostratigraphy and biostratigraphy of Cambrian Stage 3 in western Nevada and eastern California. Museum of Northern Arizona Bulletin 67, 26–42.

Hughes, N.C., 1995. Trilobite taphonomy and taxonomy: A problem and some implications. PALAIOS 10, 283–285.

Karlstrom, K., Hagadorn, J., Gehrels, G., Matthews, W., Schmitz, M., Madronich, L., Mulder, J., Pecha, M., Giesler, D., Crossey, L., 2018. Cambrian Sauk transgression in the Grand Canyon region redefined by detrital zircons. Nature Geoscience 11, 438–443.

Kidwell, S.M., Best, M.M., Kaufman, D.S., 2005. Taphonomic trade-offs in tropical marine death assemblages: Differential time averaging, shell loss, and probable bias in siliciclastic vs. carbonate facies. Geology 33, 729–732.

Maloof, A.C., Porter, S.M., Moore, J.L., Dudás, F.Ö., Bowring, S.A., Higgins, J.A., Fike, D.A., Eddy, M.P., 2010a. The earliest Cambrian record of animals and ocean geochemical change. GSA Bulletin 122, 1731–1774.

Maloof, A.C., Ramezani, J., Bowring, S.A., Fike, D.A., Porter, S.M., Mazouad, M., 2010b. Constraints on early Cambrian carbon cycling from the duration of the Nemakit-Daldynian–Tommotian boundary δ^{13}C shift, Morocco. Geology 38, 623–626.

Maloof, A.C., Schrag, D.P., Crowley, J.L., Bowring, S.A., 2006. An expanded record of Early Cambrian carbon cycling from the Anti-Atlas Margin, Morocco. Canadian Journal of Earth Sciences 42, 2195–2216.

Manzuk, R.A., Singh, D., Mehra, A., Geyman, E.C., Edmonsond, S., Maloof, A.C., 2022. A high-resolution, multispectral macro-imager for geology and paleontology. GSA Today 32, 4–9.

Mehra, A., Howes, B.J., Manzuk, R.A., Spatzier, A., Samuels, B.M., Maloof, A.C., 2022. A novel technique for producing three-dimensional data using serial sectioning and semi-automatic image classification. Microscopy and Microanalysis , 1–16.

Peng, S., Babcock, L., Ahlberg, P., 2020. Chapter 19 - the cambrian period, in: Gradstein, F.M., Ogg, J.G., Schmitz, M.D., Ogg, G.M. (Eds.), Geologic Time Scale 2020. Elsevier, pp. 565–629.

Sarg, J.F., 1988. Carbonate sequence stratigraphy, in: Sea-Level Changes: An Integrated Approach. Society of Economic Paleontologists and Mineralogists.

Smith, E.F., Macdonald, F.A., Petach, T.A., Bold, U., Schrag, D.P., 2016. Integrated stratigraphic, geochemical, and paleontological late Ediacaran to early Cambrian records from southwestern Mongolia. GSA Bulletin 128, 1056–1056.

Sundberg, F., Karlstrom, K., Geyer, G., Foster, J., Hagadorn, J., Mohr, M., Schmitz, M., Dehler, C., Crossey, L., 2020. Asynchronous trilobite extinctions at the early to middle Cambrian transition. Geology 48, 441–445.

Swart, P.K., 2015. The geochemistry of carbonate diagenesis: The past, present and future. Sedimentology 62, 1233–1304.

Tessier, A., Campbell, P.G., Bisson, M., 1979. Sequential extraction procedure for the speciation of particulate trace metals. Analytical chemistry 51, 844–851.

Wagoner, J.C.V., Posamentier, H.W., Mitchum, R.M., Vail, P.R., Sarg, J.F., Loutit, T.S., Hardenbol, J., 1988. An overview of the fundamentals of sequence stratigraphy and key definitions, in: Sea-Level Changes: An Integrated Approach. Society of Economic Paleontologists and Mineralogists.